AIAA Propulsion and Energy Forum
August 9-11, 2021, VIRTUAL EVENT
AIAA Propulsion and Energy 2021 Forum

10.2514/6.2021-3405

Performance at High Current Densities of a Magnetically-Shielded Hall Thruster

Leanne L. Su* and Benjamin A. Jorns†
University of Michigan, Ann Arbor, MI, 48109

An experimental investigation was performed to characterize the relationship between performance and current density in a magnetically-shielded Hall thruster. The H9, a 9-kW class thruster, was operated from its nominal current density to 2.7× that value at a discharge voltage of 300 V. Performance measurements were taken with a thrust stand and a probe suite to characterize the anode efficiency and the various efficiency modes. It was found that the thruster operation remained stable with less than 50% peak-to-peak discharge current oscillations for all test conditions, and the thrust, specific impulse, and anode efficiency all increased with current density. A maximum power of 12 kW was reached with 700.1 mN of thrust and 65.8% anode efficiency. An analysis of different efficiency modes revealed that the mass utilization increased with current density while the voltage utilization, current utilization, and charge utilization decreased. The improvement in mass utilization was sufficient to overcome the other loss terms. These results are interpreted in the context of physical processes that may explain the observed relationship between current density and efficiency. Challenges and potential mitigation strategies with scaling to higher current density are also discussed.

Nomenclature

α	Thruster specific mass
β	Electron temperature correctional factor for plasma potential
$\dot{m}_a$	Anode neutral mass flow
$\dot{m}_b$	Beam ion mass flow
η_b	Beam current utilization efficiency
η_b	Mass utilization efficiency
η_d	Plume divergence efficiency
η_q	Charge utilization efficiency
η_v	Voltage utilization efficiency
$\eta_{a,probe}$	Anode efficiency as measured by probe suite
$\eta_{a,thrust}$	Anode efficiency as measured by thrust stand
η_{tot}	Total efficiency
γ_i	i^{th} secondary electron emission coefficient
κ_G	Probe correctional factor
κ_{SEE}	Secondary electron emission correctional factor
λ_{iz}	Ionization mean free path
$\mathcal{T}$	Thrust
ν_{en}	Electron-neutral collision frequency
ν_{iz}	Ionization frequency
Ω_i	i^{th} current fraction
ω_{ce}	Electron gyrofrequency
ϕ_f	Floating potential
ϕ_p	Plasma potential
σ_{en}	Electron-neutral collision cross-section
σ_{iz}	Ionization cross-section
θ_d	Plume divergence angle

*Ph.D. Candidate, Department of Aerospace Engineering, AIAA Student Member
†Assistant Professor, Department of Aerospace Engineering, AIAA Associate Fellow

A_C	Collector area
A_w	Thruster wall area
B	Magnetic field strength
B_0	H9 nominal magnetic field strength
d	Thruster diameter (distance between channel centerlines)
D_T	H9 thruster diameter
g_0	Gravitational constant
h_C	Collector height
h_{GR}	Guard ring height
I_b	Beam current
I_d	Discharge current
I_{FP}	Current collected by Faraday probe
$I_{sp,a}$	Anode specific impulse
$I_{sp,tot}$	Total specific impulse
j	Current density
L	Thruster channel length (distance from anode to exit plane)
m_e	Electron mass
m_i	Ion mass
n_0	Plasma density
n_n	Neutral density
P_d	Discharge power
P_w	Power loss to channel walls
q	Elementary charge
R	Probe suite measurement radius
R_C	Collector radius
R_{GR}	Guard ring radius
T_e	Electron temperature
T_n	Neutral temperature
V_a	Acceleration voltage
V_d	Discharge voltage
v_e	Thermal electron velocity
v_n	Thermal neutral velocity
V_{RPA}	Voltage measured by RPA
Z_i	i^{th} charge state

I. Introduction

With recent renewed interest in nuclear electric propulsion, particularly for crewed exploration to Mars and beyond, there is a near term need to develop higher power (>1 MW) electric propulsion (EP) systems [1–3]. The high specific impulses of EP make it an attractive candidate for deep space missions, and scaling EP systems to higher powers would allow for such missions to be accomplished on reasonable time scales. Despite these compelling qualities of electric propulsion, there are a number of challenges associated with achieving these high power levels. These include questions of thruster specific mass α (kg/kW), power density (kW/m^2), and system redundancy. Most notably, as was pointed out in a study by Dankanich [4], rapid transits to Mars could require thruster specific masses lower than 0.5 kg/kW.

With these challenges in mind, there are a number of potential EP technologies that could be developed to achieve these higher powers. Historically, magnetoplasmadynamic (MPD) thruster and magnetic nozzles have been the leading candidate technologies. Their lower α translates to a smaller mass and area footprint. This advantage, however, is balanced against the relatively low technology readiness level (TRL) of both technologies. On the other hand, more mature EP technologies like Hall effect thrusters (HET) and gridded ion thrusters (GIT) have a high TRL at lower power (<10 kW). The high efficiency, moderate thrust, and decades of in-space heritage of HETs particularly favor this technology to access this power regime. However, to date, the limitations of conventional scaling laws for the design and fabrication of these devices have posed a major technical obstacle for adapting them to higher power. Due to various design limitations, Hall thrusters based on traditional scaling laws have operated at a limited thruster specific mass of ~2.4 kg/kW [5, 6]. As a result, Hall thruster size scales with power, becoming prohibitively large (over 2 m in diameter) for the 100-kW range [6]. Traditional scaling laws of Hall thruster power thus do not allow for a single HET to compete in terms of power density with technologies such as MPDs, which can reach specific masses of 0.05 kg/kW [7].

Faced with this limitation, there have been a few proposed strategies to achieve 1 MW power scaling with HETs, including arraying and channel nesting. In the former approach, a series of smaller, lower-power thrusters are operated in parallel to achieve the required higher power. The advantage of this strategy is that the power level per thruster remains relatively low (i.e. comparable to already flight-qualified levels) while the system has built in fault tolerance [5]. However, the challenge of high system specific mass and large footprint remains. The latter technique of channel nesting helps overcome some of the limitations of traditional arraying. In this case, concentric channels are placed around an internally-mounted cathode [8, 9]. By effectively splitting the power across multiple channels of different size, nesting can lower the overall system mass and footprint. For example, at the 200-kW power level, the diameter of a two-channel nested Hall thruster is approximately half that of a single-channel thruster [10]. Additionally, nested Hall thrusters offer the advantage of throttelability, as individual channels can be turned on or off to prioritize high specific impulse or high thrust. This strategy led to the creation and demonstration of the X3, a 3-channel 100-kW class Hall thruster that achieved a thrust of 5.4 N [11–16]. Although the specific mass in principle improves with nested thrusters, it is still not competitive with proposed MPD technology. Nested Hall thrusters also have a number of engineering challenges due to their complexity [15, 16]. Thus, although arraying and nesting offer viable paths to increase power system level power to achieve 1 MW, the specific mass and footprint may still be prohibitive for crewed exploration.

In light of this challenge, one approach that has been relatively unexplored to date is to revisit the assumed limitations on power density (alternatively viewed as system specific mass) in HET design. Indeed, while it is commonly accepted that there is a practical upper bound in state-of-the-art (SOA) thrusters for power density, it is not clear how inflexible this upper bound is [17]. To this point, Grishin et al. have previously successfully operated a single channel bismuth 100-kW Hall thruster with high power density [18]. This result showed that it is indeed possible to exceed traditional limits. However, we do note that this thruster ran at a discharge voltage of ~8 kV and discharge current of 12.5 A, therefore operating at a specific impulse too high for most mission spaces. More practically, for crewed exploration, we need to access lower-specific impulse (discharge voltage), higher-current density regimes. This invites key questions of what drives the limitations on current density in Hall thrusters and how they can be overcome.

Currently, typical Hall thrusters operate across a narrow range of current densities. Potential reasons for this limitation include thermal stability driven by the need for passive cooling as well as decreases in efficiency that observed at higher current density [17]. With that said, there has been some relatively recent work to suggest that there may be a potential technical path to design thrusters that push beyond these traditional limits. For example, previous studies [19] have shown that the overall efficiency may not decrease precipitously with higher current density. Additionally, these losses can be mitigated by changing thruster properties like magnetic field strength. This suggests the reduction in efficiency may not be overly prohibitive in increasing current density. In parallel with this result, the advent of magnetic shielding may help alleviate some of the thermal issues associated with scaling to higher power. Magnetic shielding is a technique that shapes magnetic field lines in the Hall thruster channel such that the impingement of energetic ions on the walls is greatly reduced [20, 21], extending thruster lifetimes. Shielding may improve high-current density operation, as one of its key features is lowering the electron temperature at the walls [22]. This could help reduce wall power losses and mitigate some of the thermal issues at higher current density.

Given these recent developments in thruster design as well as the renewed interest in higher-power, lower-specific mass technologies, the need is apparent for an experimental investigation to explore the operation of high current densities on a magnetically-shielded Hall thruster. With this in mind, the goal of this work is to characterize the operation of a 9-kW MS Hall thruster up to a current density 2.7× its nominal value at 15 A. We carry out this performance characterization with thrust and efficiency measurements in addition to metrics of thruster health, such as oscillations and temperatures. We also employ an efficiency model to evaluate how various losses change as we increase current density [23–25].

This paper is organized in the following way. In the first section, we review the physical limitations on current density, the perceived challenges with scaling, and the potential advantages that stem from magnetic shielding. In the next section, we discuss the experimental setup including the test article, facility, operating conditions, and diagnostics that we employed for performing the current density study. We then review an efficiency model we used to characterize the different contributions to performance, as well as our methods of data processing. Next, we present a summary of results, including trends in efficiency and thrust with current and how the efficiency breakdown changes as the current density is increased by a factor of 2.7 from its design value. Finally, we discuss these results in the context of what effects could be driving the observed trends efficiency and their implications for scaling single-channel magnetically-shielded Hall thrusters into even higher current densities.

II. Challenges with Increasing Hall Thruster Current Density

In this section, we discuss why Hall thrusters have not been operated at high current densities in the past, as well as potential developments that now allow us to achieve this operational regime. We will first discuss how various types of EP thrusters scale with power and the implications for their sizing at the 1-MW scale. Next, we review the physical reasons for the limitation on current density in the channel of a Hall thruster. Finally, we explore possible methods for scaling to higher current densities and how magnetic shielding may enable this.

A. Scaling of thruster size with power

A major driver for scaling to high power is the need to minimize thruster size, because smaller size and lower α enable more rapid transits. One strategy would be to simply increase the discharge voltage—however, higher voltages lead to higher specific impulses, and for the purposes of deep-space crewed missions we are more interested in higher-thrust, lower-specific impulse operating regimes. We therefore focus on increasing current density instead of voltage.

With this in mind, we show in Fig. 1 typical scaling of power for a range of state-of-the-art thruster technologies as a function of diameter. At constant discharge voltage, the power of a Hall thruster scales approximately with the diameter squared, $P_d \propto d^2$, due to the dependence of discharge current on the neutral mass flow rate which in turn is dependent on the channel area [17]. To generate the curve shown in Fig. 1, we have fit a quadratic to two moderately powered thrusters, the H9 and X3 [10, 11, 15, 26]. Similarly, gridded ion thrusters (GITs) also scale in power with diameter squared due to the space-charge-limited current. We therefore fit a quadratic to the NSTAR and NEXT-C thrusters, two SOA GITs, to generate the fitted curve.

MPDs, on the other hand, scale with diameter to the fourth due to the quadratic dependence of power on discharge current and of discharge current on thruster diameter ($P \propto I_d^2$, $I_d \propto d^2$). We have generated this curve by fitting a quartic function to two experimental MPDs with known dimensions and power levels [7, 27]. It should be noted that another candidate for a small, high-power thruster is the Variable Specific Impulse Magnetoplasma Rocket (VASIMR), an electrothermal nozzle-type thruster [28]; however, for the sake of brevity we neglect to include it in our plot.

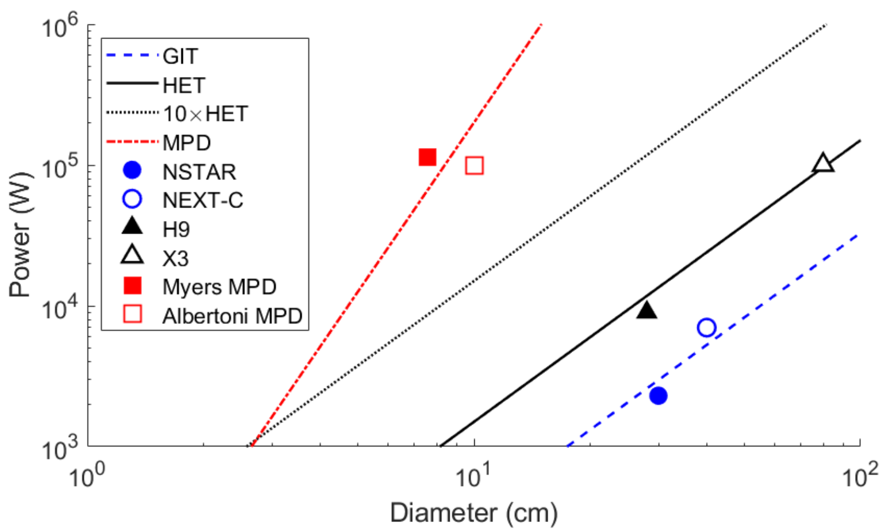

Fig. 1 Notional scaling of power (1 kW to 1 MW) with thruster size (1 cm diameter to 100 cm diameter) for gridded ion thrusters (GIT), Hall thrusters (HET), and magnetoplasmadynamic thrusters (MPD). Data taken from the NSTAR [29], NEXT-C [30], H9 [26], X3 [10, 11, 15], MPD (Myers) [27], and MPD (Albertoni) [7]. The range of specific impulses are 1500-3000 s for HETs, 2000-4000 s for GITs, and 1000-5000 s for MPDs.

As seen in Fig. 1, current SOA Hall thrusters are not able to access the same powers available to MPDs at a given size. At 100 kW, the disparity between Hall thruster and MPD sizes is an order of magnitude, with a diameter of 80 cm required for a Hall thruster but only 8 cm required for an MPD. It is ultimately for this reason that MPDs have historically been considered a more attractive technology for scaling to higher power.

If, however, we were to increase the typical current density of Hall thrusters by an order of magnitude, the disparity between Hall thrusters and MPDs correspondingly closes considerably. We represent this scaled HET notionally in

Fig. 1 with a dotted black line. At 100 kW, we would require a Hall thruster only 2−3× the size of a MPD. Especially considering the advantages of Hall thrusters over MPDs, including their heritage and high performance, this minimized size differential is likely an acceptable trade to make. With that said, as we discuss in the next section, there are physical limitations that may prevent this type of increase in HET current density.

B. Physical limits in Hall thruster current density

1. Degradation in electron confinement

One of the difficulties in scaling to higher current densities is a performance loss, believed to result from reduced confinement of the electrons in the thruster channel. The principle of operation for Hall thrusters is that we have a radial magnetic field and an axial electric field orthogonal to each other. Due to the large difference in mass between electrons and ions, the electrons are trapped in the channel spiraling along the magnetic field lines and azimuthally around the channel, while the ions are accelerated outwards by the electric field. Hall thruster operation therefore relies on strong magnetic field to impede electron current. If the electron current is too high, all the power is spent conducting this species rather than accelerating the heavier ions to generate force.

Dannenmayer and Mazouffre [17] have argued that electron confinement will decrease at higher discharge currents. To motivate this argument, we note that in order for the magnetic field to maintain strong confinement of the electrons, the electrons must be strongly magnetized, i.e.

$$\frac{\omega_{ce}}{\nu_{en}} \gg 1, \tag{1}$$

where ω_{ce} is the electron gyrofrequency and ν_{en} is the electron collision frequency. Physically, this relationship requires that collisions, which can act to allow electrons to cross field lines, are infrequent on the time scale of electron precession. The actual form of the electron collision frequency in the plasma is an active area of research in the Hall thruster community [31]; however, in order to arrive at a scaling argument, we follow Dannenmayer in assuming it scales with the electron-neutral collision frequency. This criteria then becomes

$$\frac{qB}{m_e n_n \sigma_{en} v_e} \gg 1, \tag{2}$$

where q is fundamental charge, B is the magnetic field strength, m_e is the electron mass, n_n is the neutral density, σ_{en} is the cross-section of electron-neutral collisions, and v_e is the electron thermal speed. To relate this expression to current, we invoke continuity to assume that the discharge current density scales approximately with neutral flux into the thruster:

$$j \sim q n_n v_n, \tag{3}$$

where j is the current density and v_n is the neutral thermal velocity. Substituting into Eq. 2, we find

$$\frac{q^2 B v_n}{m_e \sigma_{en} v_e} \gg j. \tag{4}$$

If we assume that neutral temperature is constant with current density and that the electron temperature is driven solely by the discharge voltage and the magnetic field, both of which we will assume remain unchanged, then we can see from Eq. 4 that there is an inherent upper bound in current density in order to ensure strong electron confinement. Physically, this relationship illustrates the fact that as current density increases, collisions in the channel increase, reducing electron confinement. It has been suggested that this relation ultimately drives the upper bound of current densities where SOA Hall thrusters operate. Beyond a certain limit, the confinement decreases, and the overall efficiency drops.

2. Thermal limitations

Another factor to consider with higher currents is the possibility of overheating due to excess power lost to the thruster body. Indeed, while state-of-the-art thrusters at lower powers are passively cooled and thermally steady, increasing the current density (and by extension power density) may lead to thermal loads that exceed the capability of standard designs to reject heat. To this point, one of the dominant loss mechanisms for Hall thrusters is electron thermal flux to the discharge chamber walls. Per Ref. [32], this power can be shown to scale as

$$P_w \propto A_w n_0 T_e^{3/2}, \tag{5}$$

where P_w is the power to the walls, A_w is the channel wall area, n_0 is the plasma density in the thruster discharge chamber, and T_e is the electron temperature immediately adjacent to the walls. As Eq. 5 shows, as plasma density increases (which for fixed discharge voltage will scale with current density), the power loss to the walls increases. To relate this to current density, we assume the conversion of all potential energy into kinetic energy and again invoke continuity to make the approximation that

$$j \sim n_0 \sqrt{\frac{2qV_d}{m_i}}, \tag{6}$$

where V_d is the discharge voltage and m_i is the ion mass. We can substitute this result into Eq. 5 to find

$$P_w \propto j A_w T_e^{3/2} \sqrt{\frac{m_i}{2qV_d}}. \tag{7}$$

Assuming the electron temperature and discharge voltage remain approximately constant as a function of current density, this result shows that as the current density increases, the power flux to the walls increases. This relationship indicates that at sufficiently high current densities, the thermal load may become prohibitive.

C. Possible strategies to mitigate limitations in increasing current density

1. Electron confinement

In order to achieve higher current, we see from Eq. 4 that a straightforward solution would be to increase the magnitude of the magnetic field strength. However, in practice, devices typically are limited in achievable magnetic field strengths. This stems primarily from the onset of saturation of magnetic materials in the magnetic circuits. On the other hand, recent studies indicate that despite the physical cap we expect at higher current densities (see Eq. 4), the hit to performance is not egregious. Work done on the H6 indicated that the current utilization efficiency from ~20 A to ~33 A decreases by about 5%, which translates to only a 2% reduction in overall total efficiency [19]. This may suggest that while an upper bound in current density likely exists, we may be able to achieve factors or even an order of magnitude of increases in current density before performance is significantly reduced.

2. Thermal effects

An unambiguous strategy to address the problem of increased thermal flux is to introduce active cooling strategies. This, however, adds an additional mass penalty that may counteract gains in thruster specific mass that stem from moving to higher current density. Alternatively, there has been recent innovations in thruster technology that may offer another potential solution, notably the advent of magnetic shielding. Magnetic shielding [20–22] presents an opportunity to mitigate some of the losses we see at higher beam currents. The nature of shielding makes it such that the electron temperatures are much lower than that of unshielded thrusters at the walls; one comparison of the unshielded H6 to the shielded H9 indicates that the wall temperatures for the unshielded case is about 17 eV while the shielded case is 3 eV [22, 33]. If we consider this factor of ~6 in electron temperature in terms of Eq. 7, we could potentially decrease the power loss to the walls by a factor of ~15 at a given current density. This in turn would allow us to significantly increase our current densities.

In summary, we have revisited some of the restrictions on current density in Hall thrusters and the challenges associated with pushing past the upper bound. The major limitations are weakened electron confinement and thermal issues with power deposited to the walls. However, recent work suggests that both may be revisited; the efficiency loss due to weakened electron confinement is not severe, and the advent of magnetic shielding may mitigate the thermal concerns at high power. We are now faced with a nontrivial question: are magnetically-shielded Hall thrusters actually capable of reaching these high current densities? If so, how does the performance trend, and how could we take steps to improve it?

III. Experimental Setup

In this section we introduce the thruster and facility used for the experiment as well as our operating conditions. We also detail the diagnostics used to collect various plasma parameters and how they were operated.

A. Test article

Our test article for this study was the H9 (Fig. 2), a 9-kW magnetically-shielded Hall thruster developed in partnership between the University of Michigan (UM), Jet Propulsion Laboratory (JPL), and the Air Force Research Laboratory (AFRL) [26, 34]. We used a centrally-mounted LaB6 cathode [35] operating at a fixed 7% cathode flow fraction with the cathode tied to the body at all conditions. Xenon was the only propellant used for this study. A number of thermocouples were attached to the H9 at various locations to monitor thruster health. We operated the H9 in the Large Vacuum Test Facility, a chamber 6 m in diameter and 9 m in length, which is capable of pumping ~500 kL/s of xenon. Pressures in the chamber were measured with a Stabil ion gauge calibrated for xenon, mounted 1 m away from the thruster in the thruster exit plane following industry standards [36].

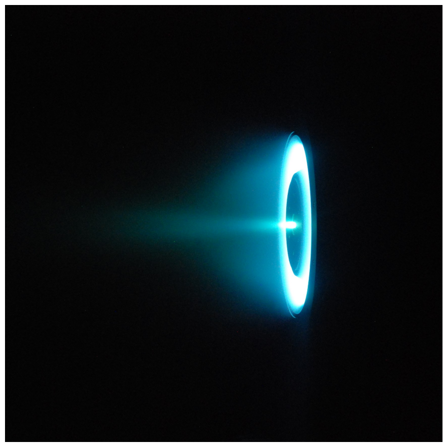

Fig. 2 H9 running at 300 V, 40 A in the Large Vacuum Test Facility.

We operated the thruster at the discharge currents shown in Table 1, keeping discharge voltage constant at 300 V. We operated all conditions at 100% B_0 and the 35 and 40 A conditions at 87.5% B_0.

Current (A)	Relative magnetic field strength	Anode mass flow (mg/s)	Facility pressure (μtorr)
15	100%	14.8	4.8
20	100%	18.6	5.8
25	100%	22.0	6.7
30	100%	25.3	7.6
35	100%	28.3	8.4
40	100%	31.1	9.1
35	87.5%	28.5	8.4
40	87.5%	31.4	9.1

Table 1 Operating conditions. Mass flows and facility pressures taken at time of thrust measurement.

B. Diagnostics

We used a null-type inverted pendulum thrust stand to measure thruster performance [37]. This thrust stand was operated in null displacement mode and calibrated by with a series of weights corresponding to expected thrusts. We note here that our calibration only extended to thrust values approximately half of the maximum thrust reported here due to limitations on the available weights (the stand is typically employed for lower power operation). We assume in this work, however, that the stand response remained approximately linear, following the same calibration range up to the values we measured. In addition to performance measurements, we also employed a set of probes including a retarding potential analyzer (RPA), emissive probe (EP), Langmuir probe (LP), Faraday probe (FP), and E×B probe to

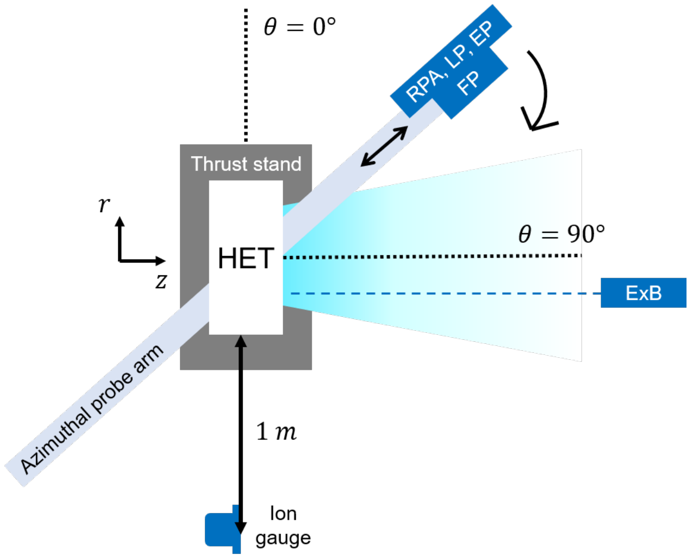

Fig. 3 Overhead schematic of experimental setup illustrating probe and thrust stand locations.

characterize the efficiency breakdown. The RPA, EP, LP, and FP were part of a probe suite mounted on a radial arm with its axis of rotation situated directly above the exit plane of the thruster. These probes collected data at a location 10.25 thruster diameters (D_T) downstream. The RPA, EP, and LP each collected data at 90 degrees, directly facing the centerline of the thruster, while the FP performed two sweeps from 0 to 180 degrees and back again with data being collected every ~1 degree. The E×B probe was mounted about 12 D_T downstream of the thruster, aligned to the channel centerline.

The RPA we employed had a 6.45 cm^2 aperture with four grids and a collector inside. We set both the primary and secondary electron suppression grids to -30 V and swept the ion selection grid from 0 to 600 V. The emissive probe we used was comprised of a thin loop of 1 mm length thoriated tungsten filament wire, heated to thermionic emission such that the potential approached the plasma potential. We employed a Langmuir probe consisting of a 4 mm length of tungsten wire routed through a ceramic tube, and we swept the bias voltage from -5 to 15 V. The Faraday probe used to measure ion saturation current had a 1.74 cm inner diameter molybdenum collector and 2.38 cm outer diameter molybdenum guard ring, with a 0.05 gap between them, and was biased to -30 V during probe sweeps. The E×B probe had an entrance aperture 1.6 mm in diameter, an entrance collimator 7.5 cm long, an exit collimator 15 cm long, and electrical plates spaced 0.97 cm apart. The peak magnetic field was 0.16 T in the center of the probe. We swept the applied bias voltage to the plates from 0 to 80 V.

IV. Efficiency Model

Having established the experimental setup, we can now describe the model we use to evaluate performance metrics of our thruster. In this work, we directly calculate the anode efficiency η_a from performance measurements of thrust $\mathcal{T}$, and operating parameters of anode mass flow $\dot{m}_a$ and discharge power P_d. Thrust and anode mass flow are also used to determine the anode specific impulse, $I_{sp,a}$. The "total" values of efficiency and specific impulse use $\dot{m}_{tot}$ and P_{tot} in place of $\dot{m}_a$ and P_d, respectively. We further try to explain the trends in these measured efficiencies by considering its various contributions. This breakdown is based on the Hall thruster efficiency model developed by Hofer [23–25, 32], which defines the anode efficiency as the product of the five contributions:

$$\eta_a = \eta_b \eta_v \eta_d \eta_q \eta_m, \tag{8}$$

where η_b is the current utilization efficiency, η_v is the voltage utilization efficiency, η_d is the plume divergence efficiency, η_q is the charge utilization efficiency, and η_m is the mass utilization efficiency. Each of these contributions can be inferred from measurements of the plume properties of the plasma. In particular, we have the following definitions:

- *Current utilization efficiency*: The fraction of ion current contained in the discharge current is defined as

$$\eta_b = \frac{I_b}{I_d}, \tag{9}$$

where I_d is the discharge current and I_b is the ion beam current.

- *Voltage utilization efficiency*: The conversion of voltage into ion velocity is defined as

$$\eta_v = \frac{V_a}{V_d}, \tag{10}$$

where V_d is the discharge voltage and V_a is the average acceleration voltage.

- *Plume divergence efficiency*: The decrease in axially-directed momentum from divergence of the ion beams is defined as

$$\eta_d = (\cos\theta_d)^2, \tag{11}$$

where θ_d is the angle of plume divergence from channel centerline.

- *Charge utilization efficiency*: The decrease in efficiency from multiply-charged ions in the beam is defined as

$$\eta_q = \frac{\left(\sum_i \frac{\Omega_i}{\sqrt{Z_i}}\right)^2}{\sum_i \frac{\Omega_i}{Z_i}}, \tag{12}$$

where Ω_i is the current fraction of the i^{th} charge ion species, $\frac{I_i}{I_d}$, and Z_i is the charge state of the i^{th} ion species.

- *Mass utilization efficiency*: The conversion of neutral mass flux into ion mass flux is defined as

$$\eta_m = \frac{\dot{m}_b}{\dot{m}_a} = \frac{\frac{m_i I_b}{q}\sum_i \frac{\Omega_i}{Z_i}}{\dot{m}_a} = \xi\eta_b \sum_i \frac{\Omega_i}{Z_i}, \tag{13}$$

where $\dot{m}_a$ is the neutral anode mass flow rate, $\dot{m}_b$ is the ion beam mass flow rate, m_i is the ion mass, and ξ is a value defined as the exchange ratio.

We can use this model for the breakdown of the anode efficiency to identify what specific processes within the thruster are primarily contributing to losses. By measuring each of these efficiency components, we can also compare the anode efficiency calculated by taking the product of all five efficiency modes $\eta_{a,probe}$ to the anode efficiency calculated with the thrust, anode mass flow rate, and discharge power, $\eta_{a,thrust}$. To evaluate these terms, we use the types of plume data described in the next section.

V. Methodology for Data Analysis

In this section, we talk about how we use our various probe measurements to calculate key plasma parameters. These values include plasma potential, electron temperature, charge states, beam current, and divergence angle. For each set of values, we present a trace at the lowest and highest current values (15 and 40 A, respectively).

A. Average ion energy

To measure the average ion energy, we combined measurements from the RPA, EP, and LP. First, from the RPA, we generated an ion energy distribution function (shown in Fig. 4). These plots indicate the probability of energy as function of charge to mass ratio. From this, we extracted the most probable value for voltage along centerline by finding the peak of each trace. The RPA is referenced with respect to ground, so we need the local plasma potential to convert to kinetic energy. We therefore need additional plasma parameters to calculate the acceleration voltage shown in Eq. 10:

$$\phi_p = \phi_f + \beta T_e, \tag{14}$$

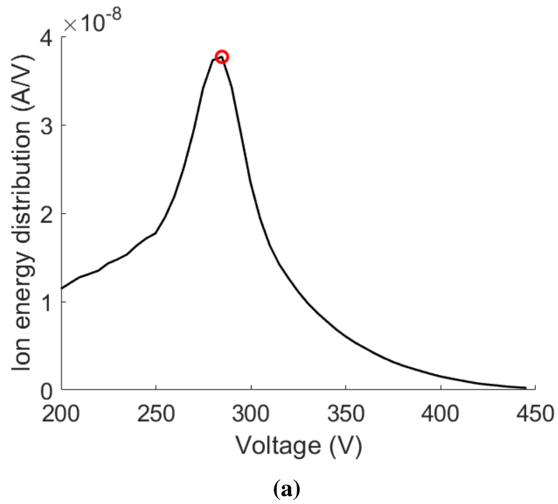

Fig. 4 Ion energy distribution functions for a) 300 V, 15 A and b) 300 V, 40 A as measured by the RPA, correcting for the plasma potential as calculated per Eq. 15 from the emissive and Langmuir probes.

$$V_a = V_{RPA} - (\phi_f + \beta T_e), \tag{15}$$

where ϕ_p is the plasma potential, V_{RPA} is the voltage measured by the RPA, ϕ_f is the floating plasma potential measured by the EP, T_e is the electron temperature measured by the LP, and β is a correctional factor ranging from 0 to 1.5, where 0 was used to set a lower bound and 1.5 used to set an upper bound for the plasma potential [38, 39]. The average of this upper and lower bound is taken as the value for acceleration voltage, with the standard deviation determining 95% confidence intervals. We determine the most probable voltage along centerline from the RPA by locating the maximum in the derivative of the current trace.

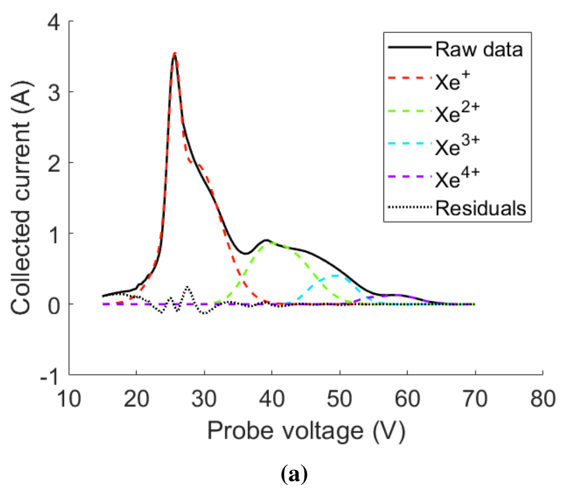

Fig. 5 Raw E×B traces taken at a) 300 V, 15 A and b) 300 V, 40 A.

B. Charge states

For the current collected by the E×B probe, we use a series of four two-peak Gaussian fits to determine the ratio of each current species Ω_i. This fit has previously been shown to accurately capture the distribution of each species [40]. Additionally, the two-peak Gaussian specifically proved to be the best fit during the analysis process as determined by residuals, defined as the resultant curve after subtracting the fitted two-peak Gaussians from the raw trace [33]. We calculate charge fractions by integrating the area under each fit and comparing it to the total integrated area under the curve, and quantify uncertainty by integrating under the absolute value of the residuals associated with each curve.

C. Beam current and divergence angle

We determine the beam current by measuring the current density at different locations downstream with the FP. A correctional factor κ_G is used to account for the gap between the FP collector and guard ring. Secondary electron emission (SEE) coefficients γ for xenon and krypton are used in conjunction with the charge fractions determined by the E×B probe to correct for secondary electron emission in the current density trace with the correctional factor κ_{SEE}. These correctional factors are defined in Ref. [41] as:

$$\kappa_G = \pi(R_{GR}^2 - R_C^2)\left(\frac{2\pi R_c h_C}{2\pi R_C h_C + 2\pi R_{GR} h_{GR}}\right), \tag{16}$$

where R_{GR}, R_C, h_{GR}, and h_C are the radii and heights of the guard ring and collector, respectively, and

$$\kappa_{SEE} = \frac{1}{1 + \sum_i \frac{\Omega_i \gamma_i}{Z_i}}, \tag{17}$$

where γ_i is the SEE coefficient of the i^{th} charge state, and Z_i is the i^{th} charge state from 1 to 4. The ion current density j is then calculated as follows [41]:

$$j = \frac{I_{FP}}{A_C + \kappa_G} \kappa_{SEE}, \tag{18}$$

where I_{FP} is the raw current calculated by the Faraday probe and A_C is the collector area.

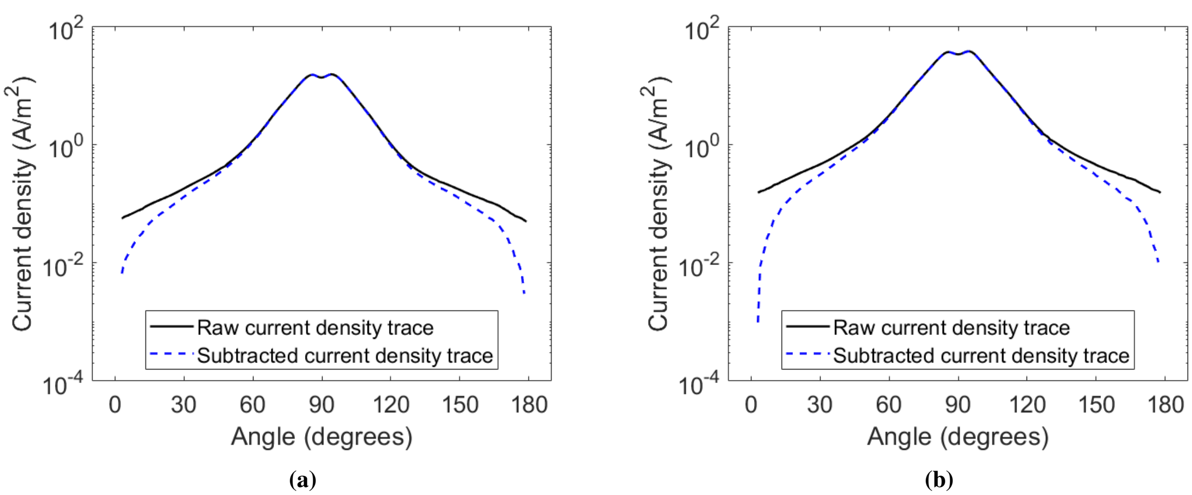

Fig. 6 Current densities calculated from Faraday probe traces per Eq. 18 at a) 300 V, 15 A and b) 300 V, 40 A.

The values for the first and second charge states are determined by averaging γ from 100 to 1000 eV, following methods outlined in best practices for Faraday probes [41], from measurements of xenon and krypton impinging on molybdenum [42]. The third and fourth charge state use ratios of higher γ to lower γ for tungsten [43], as these ratios were not measured for molybdenum. We assume the ratios to be the same for molybdenum to extrapolate the 1st and 2nd charge state γ values. We can then calculate the beam current I_b and divergence angle θ_d as:

$$\cos\theta_d = \frac{\int_0^{\pi/2} j(\theta)\cos\theta\sin\theta\, d\theta}{\int_0^{\pi/2} j(\theta)\cos\theta\, d\theta}, \tag{19}$$

$$I_b = 2\pi R^2 \int_0^{\pi/2} j(\theta) \cos\theta \, d\theta, \tag{20}$$

where R is the distance from the exit plane of the thruster to the probe and θ is the azimuthal location of the probe in radians. Ideally, we would use a linear fit for divergence angle to the exit plane of the thruster to determine its true value [41]; this methodology was applied to the 15 A and 20 A conditions. However, for our work, we only have one distance for our Faraday measurements for the high-current condition at 40 A. From the data we had previously taken at 15 A and 20 A, we saw that the divergence angle at the exit plane was 76%-78% the value at 10.25 D_T. We therefore estimate the divergence angle for the 40 A condition based on this ratio and take the error to be the difference between that value and the raw value we measured at 10.25 D_T.

Due to the preferential collection of slow CEX ions over fast beam ions [44], the FP trace has an artificially high measurement in the wings. Multiple methods of accounting for this discrepancy have been proposed [40, 45], but many of them are to extrapolate to zero-pressure while our goal is to characterize performance at our lowest finite background pressure. We therefore use a rough estimate of an upper and lower bound for our beam current calculations, resulting in large uncertainty intervals. The integrated value of I_b of the raw trace is treated as the upper bound for the beam current. For the lower bound, we subtract off the value of j at the point furthest away from centerline (i.e. 0 or 180 degrees), assuming that any charge collected there is purely due to ambient ions. The average values and uncertainties of I_b are then determined by the mean and standard deviation between upper and lower bounds for beam current.

The beam ion mass flow rate and mass utilization efficiency are calculated with the discharge current as measured by the data acquisition system, beam current as determined by the FP, and ratios of charge species as determined by the E×B probe in accordance with Eq. 13. The uncertainty from all individual measurements are propagated through to the final value of η_m. The product of the individually-calculated efficiencies is taken to be the "probe-calculated" anode efficiency, $\eta_{a,probe}$, as shown in Eq. 8. Having established the methodology we use to process our data, we now present the results from our experiment.

VI. Results

In this section, we review our findings for thermal stability and thruster performance while operating the thruster over its full range. We then leverage the plume measurements described in Sec. V to calculate the efficiency breakdown at 40 A using the model detailed in Sec. IV.

A. Thruster temperature and stability

Current (A)	Peak-to-peak current (A)	Discharge oscillations
15	7.5	50%
20	6.0	30%
25	7.0	28%
30	8.8	29%
35	11.3	32%
40	15.3	38%
35	10.7	31%
40	12.5	31%

Table 2 Operating currents and discharge oscillations. The uncertainty in peak-to-peak current is approximately ±1 A.

At each current condition, we recorded the peak-to-peak and root-mean-square of discharge current oscillations and found that these oscillations were minimized at the nominal magnetic field strength for current values of 15 A to 30 A, and at 87.5% of nominal magnetic field strength B_0 for 35 A and 40 A (Table 1). We maintained stable operation—defined in this case as exhibiting lower than 100% oscillations—at all conditions up to 40 A.

In terms of the thermal stability, during operation of the thruster, we defined a critical upper bound in temperature as the point after which we suspect the magnetic properties of the material start to degrade. We assigned this a value of ~475° C at the thruster inner screen. We plot the results as a function of time in Fig. 7. Note here that the thruster was on for eight hours during warm up and outgassing before any telemetry was collected. Additionally, the thruster was gradually increased from 15 A to 40 A in the hour before we began recording the temperatures shown in Fig. 7.

Data taken from the thermocouples showed that the temperatures never reached the critical temperature over 45 minutes of operation at the 40 A condition. This was sufficient margin for us to perform both probe and performance measurements. We note, however, that as the figure shows, the temperature had not reached equilibrium but was continuing to climb. This indicates that the thruster for long term operation may exceed the thermal margin. We return to this point in Sec. VII, where we discuss the implications for the behavior of the temperature over time.

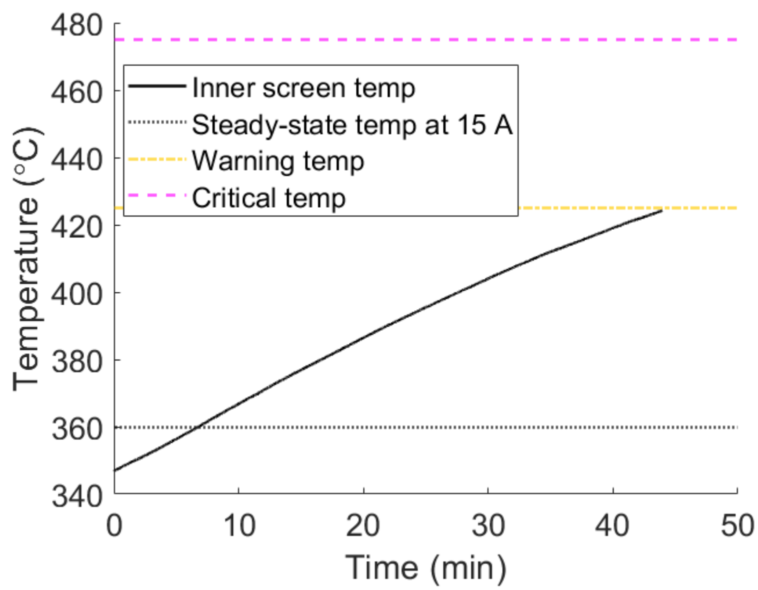

Fig. 7 Temperature variation of the inner screen over 45 minutes of continuous operation at 300 V, 40 A, compared to the steady-state value at 300 V, 15 A and the warning/critical temperatures for operation.

B. Overall thruster performance

Figure 8 shows the thrust, thrust-to-power ratio, specific impulse, and efficiency measured on the H9 at various conditions. The thrust and specific impulse both increased about linearly with current, in line with previous observations of Hall thruster trends [19]. At the 100% B_0 condition, the thrust reached a maximum of 700.1 ±5.0 mN and the total specific impulse reached a maximum of 2150 ±20 s. The anode efficiency slightly decreased from 15 to 20 A, then monotonically increased with current from 20 to 40 A, although the rate of increase slowed down at higher currents. The 87.5% B_0 condition performed slightly worse than the 100% B_0 condition at the same current conditions, although the values were still within uncertainty. The anode efficiency reached a maximum of 65.8 ±0.9% at the 40 A condition.

We can see from Fig. 8b that the thrust-to-power ratio consistently decreased with rising current. This matches trends previously seen in Reid's work on the H6 at high currents [19]. One difference to note is the lower thrust-to-power (T/P) ratios seen for the H9 in comparison to the H6—at 300 V, the H6 had T/P ratios of 60-70 mN/kW, while the H9 had T/P ratios of 57-66 mN/kW. This lower T/P ratio is a trade-off for the higher total specific impulses observed on the H9, ranging from 1850-2150 s, while the H6 values ranged from 1100-2000 s.

The major finding from our overall performance results is that the efficiency does not in fact decrease over the 15 A to 40 A current range. Instead, it remains fairly stable and actually improves by about 2-4% between 20 and 40 A. The specific impulse and thrust also increase throughout the operating range.

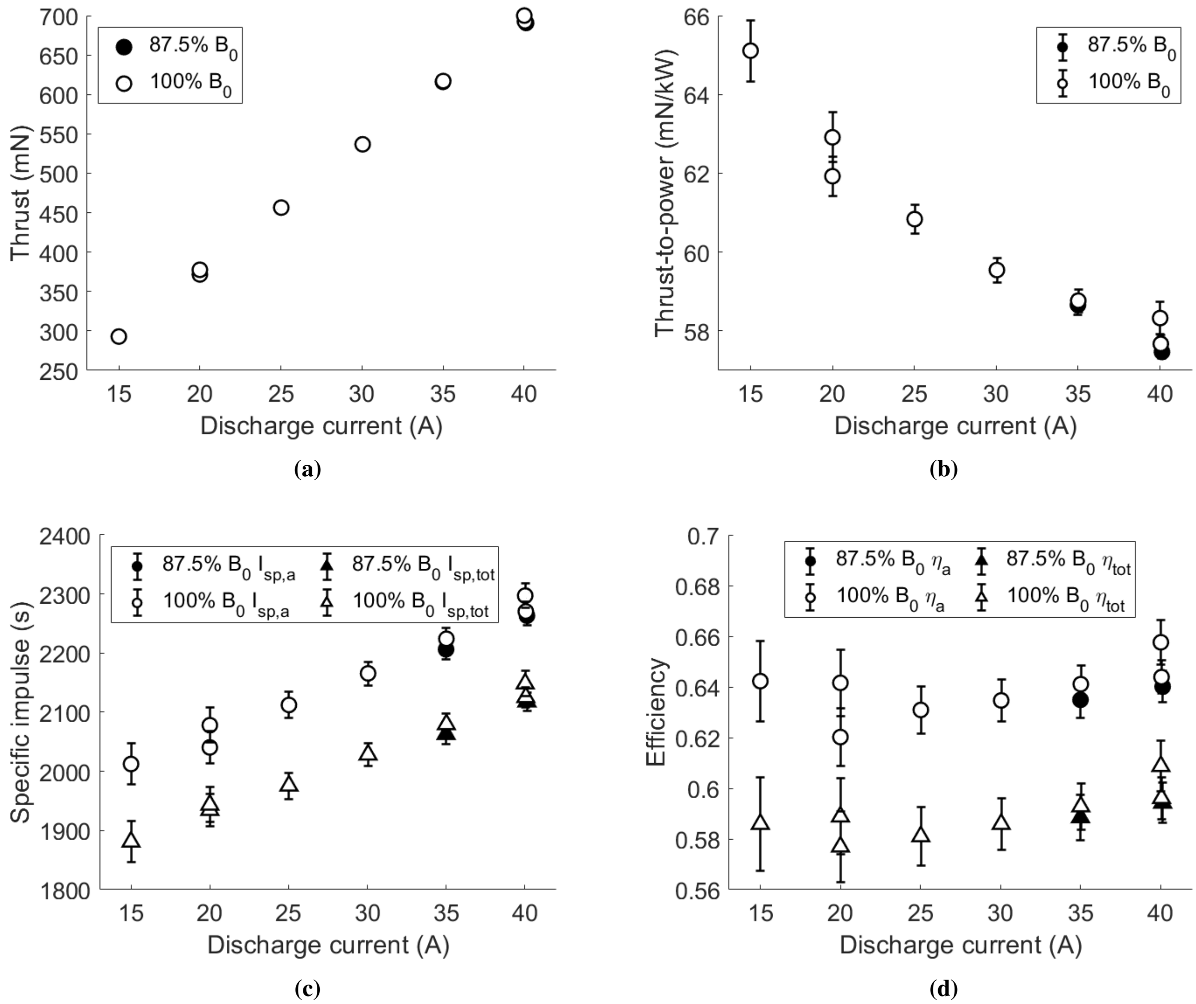

Fig. 8 a) Thrust, b) thrust-to-power ratio, c) anode and total specific impulse, and d) anode and total efficiency with varying discharge current. Note that the uncertainties on Fig. 8a are smaller than the point sizes.

C. Efficiency breakdown

We next turn to the question of why the efficiency behaves in the way we measured. To this end, we employ the efficiency model and data processing methodology previously described. Figure 9 shows the various efficiency contributions plotted parametrically as a function of discharge current.

At the highest-current condition of 40 A, the lowest efficiency mode is current utilization, 83.8 ±3.7%, and the highest efficiency mode is mass utilization, 103 ±15%. Although there are large uncertainties on the mass utilization, we still expect that this increasing trend should hold true due to a shorter ionization mean free path in the channel and therefore higher ionization, a concept that we will discuss further in Sec. VII. We may be able to explain the non-physical value of 103% for the anode efficiency at 40 A by noting the relatively high facility pressure of 9.1 μtorr (Tab. 1) at this condition. As the facility pressures increase, which is the case due to the higher flow rates required to reach higher currents, the mass utilization increases as well due to ingested neutrals from the facility [46]. Despite the large uncertainties on the probe-calculated anode efficiency relative to the mean values (15-30% error), we see that they match the thrust-calculated anode efficiencies to within 2-4% across all conditions.

Comparing the efficiency breakdown at 40 A to the 15 and 20 A conditions lends more insight into how efficiencies change with current, as seen in Fig. 9. Although the thrust-calculated efficiency increases, the trend in probe-calculated efficiency is more difficult to characterize due to the large margins of error. This is partially due to the limited data (approximate ratio instead of linear fit) used to calculate the divergence angle of the 40 A condition. We therefore speculate that the true divergence efficiency may be on the higher side of the error bar; indeed, considering the non-physically high value of 103% for the mass utilization, one or more of the other efficiency modes are likely higher than the mean for the probe-calculated efficiency to match the thrust-calculated value.

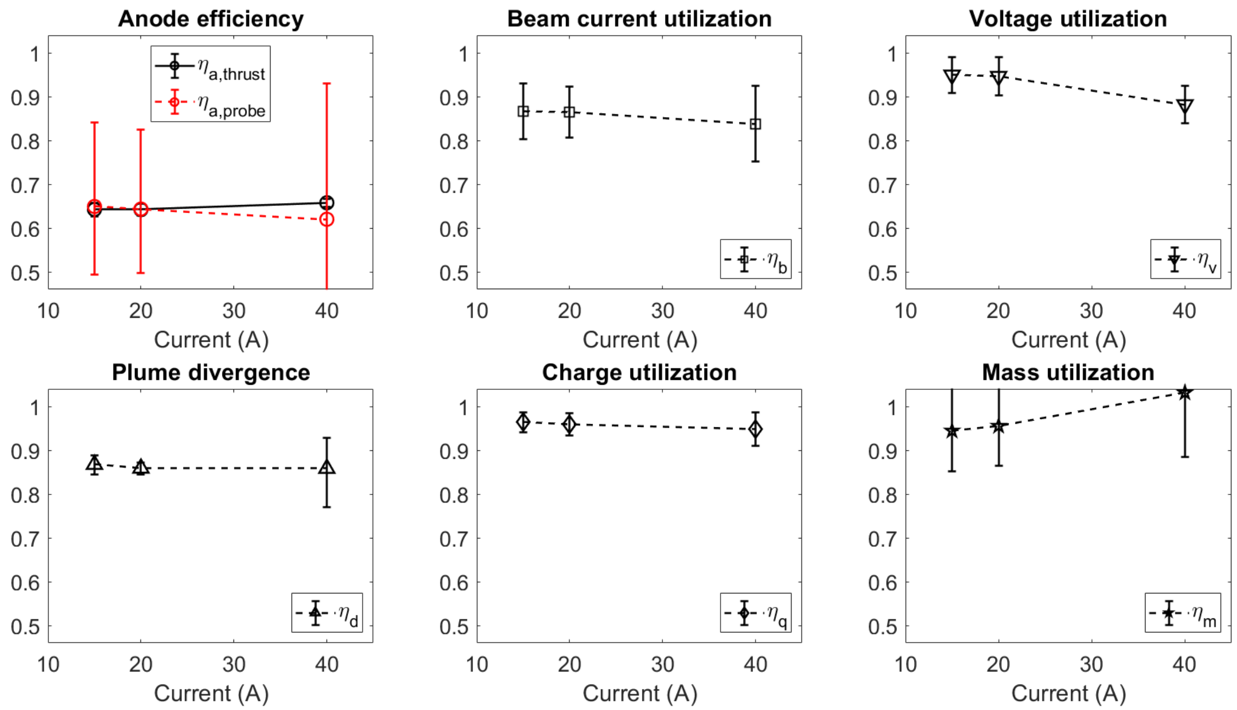

Fig. 9 Trends in various efficiencies with current.

Despite the large uncertainties, we can still characterize some trends in the efficiency modes. The charge, voltage, and beam utilization efficiencies decrease from 15 A to 40 A, while the mass utilization efficiency increases. The increase in η_m is difficult to characterize due to the large error bars; however, we can still observe that the average value increases by 9% from 15 A to 40 A. The current utilization decreases by 3%, the voltage by 7%, and the charge by 1%. These results explain the trends we see in Fig. 8. Although multiple efficiency modes decrease with current (including the beam utilization, which has been a point of concern historically), the increase in mass utilization efficiency is enough to balance out this decrease. We therefore end up with a relatively constant efficiency between 62% and 66% from 15 to 40 A.

VII. Discussion

In the following sections, we discuss the implications of our results in terms of why we observe the trends we do and how they may scale to higher powers. We first detail how we could extrapolate the thermal behavior of our thruster to a longer period of operation. Next, we discuss overall trends in performance, what efficiency modes are driving these trends, and what the physical mechanisms behind them may be. Finally, we explore possible mitigation strategies for operating safely at even higher current densities while maintaining high efficiencies.

A. Thermal stability for longer duration operation

As we discussed in Sec. VI, while the temperature remained below the critical value for the duration of the test, the temperature continued to rise (Fig. 7). This invites the question as to whether the system would actually reach a thermal steady-state that does not exceed the upper bound. To evaluate this possibility with an approximate scaling, we assume that the heat transfer at the inner screen is solely from 1D conduction. We therefore have the following form for temperature change:

$$\frac{\partial T}{\partial t} = c_0(T_0 - T), \tag{21}$$

where c_0 is a constant and T_0 is the steady-state temperature. We then know that the form of the temperature variation is:

$$T = T_0 - c_1 \exp(c_2 t), \tag{22}$$

where c_1 and c_2 are constants and t is time. We can fit this expression to the data from our experiment. As can be seen from the fit in Fig. 10, if the temperature varies exponentially, the thruster will exceed the critical temperature after about 1.5 hours of operation and eventually reach ~550 °C. However, it should be noted that this is an upper limit on estimation for the temperature over time. We neglect radiative cooling and cooling via conduction to other test infrastructure. Additionally, the H9 has been successfully operated at these higher temperatures before (up to ~500°C [33]), so there may be some margin even above our critical temperature.

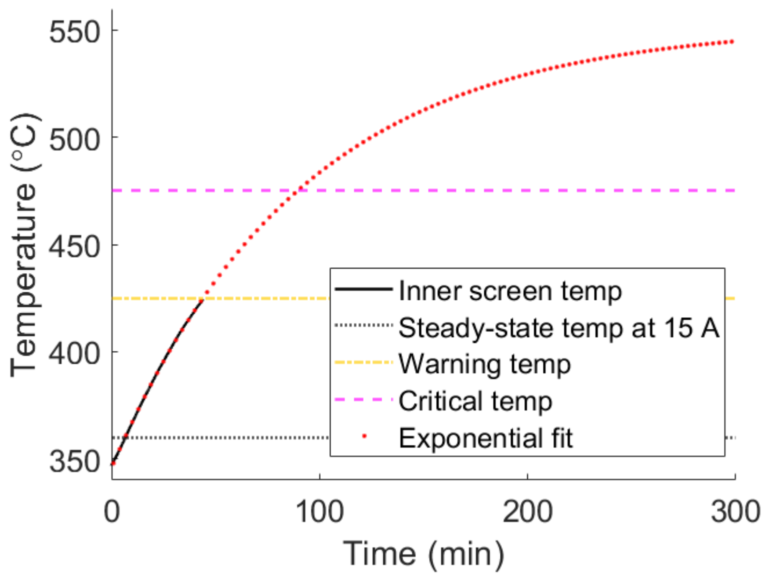

Fig. 10 Temperature variation of the inner screen over 45 minutes of continuous operation at 300 V, 40 A, compared to the steady-state value at 300 V, 15 A and the warning/critical temperatures for operation (Fig. 7). Fitted values indicate extrapolated behavior to five hours.

Despite the potentially unsustainable temperatures that we may see at higher current densities, we did not encounter any thermal issues during the duration of the test. We speculate that an unshielded thruster operating at the same current densities may not have been able to operate for the same amount of time that the H9 did without reaching dangerously high temperatures. Previous work on the H6 indicated that at the same location, the shielded configuration had temperatures ~60-80°C lower than the unshielded configuration [22]. Based on this temperature differential, we would have expected an unshielded version of the H9 to reach the critical temperature by the end of our 45-minute operation period as seen in Fig. 10.

B. Overall trends in performance

The operation of the H9 was stable and had anode efficiencies above 60% at current densities up to and including the 40 A condition. The thruster temperatures remained well below critical values during testing (Fig. 7), though there may be some thermal concern over longer periods of operation. Although the thrust-to-power ratio decreased, all other overall performance metrics—thrust, specific impulse, and efficiency—increased. Previously observed operation on unshielded thrusters showed the total efficiency stagnating/slightly decreasing at higher currents. However, as we can see in Fig. 8d, the 100% B_0 mostly increases from ~58% at 15 A to ~61% at 40 A. The trend in operation of this Hall thruster compared to an unshielded one may indicate that electron losses are less severe in shielded Hall thrusters than in unshielded.

The continually-increasing specific impulse is somewhat unexpected; historically, high-power Hall thruster specific impulses tend to plateau at higher currents [19, 47]. The linear behavior of the specific impulse increase can be attributed to the behavior of the mass utilization efficiency, which we can better understand by exploring the relationship between specific impulse and various efficiency modes. The anode specific impulse is dependent upon thrust T, flow rate $\dot{m}_a$, and gravitational constant g_0:

$$I_{sp,a} = \frac{\mathcal{T}}{\dot{m}_a g_0}. \tag{23}$$

We also know that thrust is related to the mass flow rate of the beam ions, the exit velocity, and the divergence angle, $T = \dot{m}_b\ u_e \cos(\theta)$. By casting thrust in terms of beam flow rate and charge state and assuming that all of the electric potential energy in the acceleration region is converted into kinetic energy, we can define thrust as

$$\mathcal{T} = \sqrt{\frac{2m_i V_a}{e}} I_b \cos\theta_d \sum_i \frac{\Omega_i}{\sqrt{Z_i}}. \tag{24}$$

We can then plug Eq. 24 back into Eq. 23 and cast it in terms of efficiencies as defined in Section IV:

$$I_{sp,a} = \frac{\sqrt{2qV_d}}{\sqrt{m_i} g_0} \sqrt{\eta_v \eta_d} \eta_m \eta_q. \tag{25}$$

Equation 25 indicates that at a constant voltage, the specific impulse scales with the square root of voltage and divergence efficiency, but linearly with mass efficiency. This explains why we see a steadily-increasing trend in our specific impulse—our mass utilization increases by about the same amount that our voltage utilization decreases, but the scaling factor means that the overall specific impulse still scales linearly with current densities.

C. Physical significance of trends in efficiency

The overall trend in efficiency, as seen in Fig. 8d, is relatively stable with a slight increase. This can be attributed to the increasing value of η_m—even though the charge, current, and voltage utilization efficiencies decrease, the increase in mass utilization is sufficient to overcome this deficit. In the following discussion, we will explore why each efficiency trends in the way it does.

To understand the increase in mass utilization, we first introduce the Melikov-Morozov criterion [48]:

$$\lambda_{iz} \ll L, \tag{26}$$

where λ_{iz} is the mean free path of ionization in the channel and L is the channel length. This criterion must be fulfilled in order for there to be sufficient ionization happening over the length of the channel. The ionization frequency is

$$\nu_{iz} = n_n\ \sigma_{iz}(T_e)\ v_e(T_e), \tag{27}$$

where σ_{iz} is the ionization cross-section. The ionization length can be approximated as the thermal velocity of neutrals divided by the ionization frequency:

$$\lambda_{iz} \approx \frac{v_n(T_n)}{n_n\ \sigma_{iz}(T_e)\ v_e(T_e)}, \tag{28}$$

where T_n is the neutral temperature. By relating our expression for the ionization mean free path back to the Melikov-Morozov criterion, we obtain the following relation that Dannenmayer et al. arrived at [17]:

$$\lambda_{iz} \approx \frac{v_n(T_n)}{n_n\ \sigma_{iz}(T_e)\ v_e(T_e)} \ll L. \tag{29}$$

We can now see why the ionization and mass utilization increase with increasing neutral density—as n_n increases, the ionization mean free path λ_{iz} decreases and becomes even smaller relative to the channel length. This formulation is limited, however, by an upper bound in neutral density, after which electron transport (which is neglected in Eq. 29) becomes a driving factor [17].

Interestingly, we see that the mass utilization efficiency approaches unity at around 40 A, supported by both the high η_m calculated here (Fig. 9) and the slower increase in anode efficiency at higher current densities (Fig. 8d). This maximum in efficiency indicates that the ionization mean free path is small enough that all of the available propellant in the channel is being effectively ionized. As previously discussed, the non-physical value of 103% for mass utilization efficiency at 40 A may be due to neutral ingestion from high facility pressures.

The decrease in charge utilization with current is explained by the higher ion-to-neutral density at increasing currents. As the mass utilization increases, the portion of the population within the channel that is ionized increases as well. Since higher charge states require ions to collide with electrons, a larger presence of ions within the plume will also result in more frequent higher ionization events as the ionization mean free path between ions and electrons (as opposed to neutrals and electrons) is decreased. Figure 11 shows the variation in charge species ratio at different operating currents.

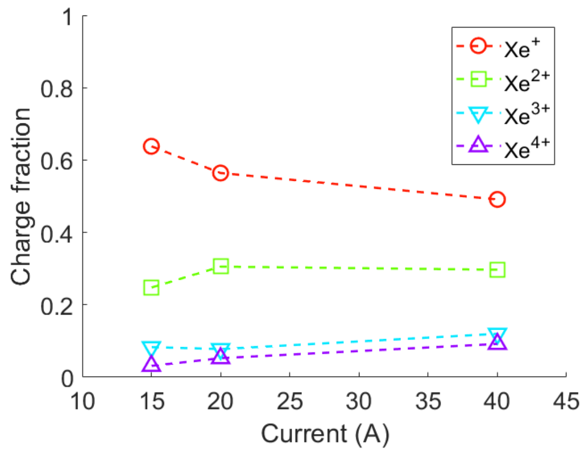

Fig. 11 Comparison of E×B charge fractions at various current conditions.

The beam utilization decreases with current density, matching trends seen in previous work [19]. This can be understood in the context of the scaling law we derived in Eq. 4. Higher current density leads to more electron transport as the magnetic field is no longer able to sufficiently confine this species. We therefore see more losses due to electron transport at higher current densities, manifesting in a lower beam current and therefore lower current utilization efficiency. We do note that the decrease in beam utilization from 1× to 2.7× nominal current density is on average about 3%, a relatively minor driver of decreasing efficiency overall.

The plume divergence stays largely unchanged. This appears to indicate that the position of the acceleration region is unaffected by current density. Higher neutral densities at the exit plane should push the acceleration region upstream [37], but the neutral density and the plasma density inside the channel scale up as well. This may result in self-similar behavior that leaves the position of the acceleration region unaffected. We should note that the large error bars on the 40 A condition and mismatch between thrust-calculated and probe-calculated anode efficiencies here (Fig. 9) may indicate that the divergence angle should be lower than the mean value, giving us a higher divergence efficiency.

The largest drop in efficiency actually comes from the voltage utilization as seen in Fig. 9. We also note that we do not see a decreasing trend between 15 A and 20 A, but instead only a stark drop in acceleration voltage by about 20 V from 20 A to 40 A. One theory for the cause of this phenomenon is that electrons are harder to extract from the cathode at higher flow rates. To investigate this theory, we compared the plasma potential calculated with Eq. 14 to the cathode-to-ground voltage of the thruster measured throughout testing. The resultant cathode coupling voltage (the potential between the plasma and the cathode) is shown in Fig. 12. The trend in cathode coupling voltage indicates that, in contrast with our hypothesis, the electrons are actually easier to extract at higher currents; ~20 V is required at the 15 and 20 A condition, while only ~16 V is required at the 40 A condition.

Another theory is that we have ions born further down the potential well in the ionization region, resulting in slower ions and therefore a lower voltage utilization. This is perhaps our most promising theory, as it is supported by the shape of the ion energy distribution functions (IEDFs) seen in Fig. 4. The shape of the IEDF for the 40 A condition has a significantly broader peak than that of the 15 A condition. This suggests that the ionization region is wider and/or has a larger overlap with the acceleration at the higher-current condition, creating lower-energy ions past the peak of the potential drop. This stretching of the ionization region may be due to the increased neutral flow into the channel—since there is more ionization happening in general (as evidenced by our increasing mass utilization efficiency), it may be taking place over a larger region spatially.

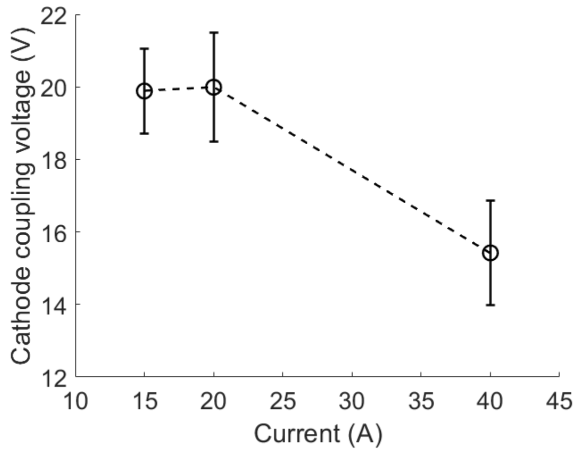

Fig. 12 Comparison of plasma to cathode potential at various current conditions.

D. Implications and strategies for extending to higher current densities

One of the most promising results of this study is that we have shown how the overall performance of the thruster, as represented by the efficiency, seems relatively unaffected as the current density is increased by a factor of 2.7 from the nominal value. With that said, as we outlined in Sec. II, in order to be competitive with MPDs, our target would be an increase of at least a factor of 10 in this value. This begs the question as to how thruster performance will change at higher current density.

To this point, we recall that despite the decreases in current, voltage, and charge utilization, the anode efficiency overall increases as shown by the $\eta_{a,thrust}$ measurement. This is due to the increasing mass utilization, which approaches unity at 40 A. Based on these trends, 2.7× the nominal current may actually represent a maximum achievable value since the mass utilization efficiency cannot continue to increase. Assuming that the observed trends in Fig. 9 hold, the other efficiency factors will only drive overall performance down as we continue to increase current density.

The possibility of a maximum in efficiency with current is consistent with previous work on unshielded thrusters. Studies on the H6 showed, for example, an efficiency peak at a discharge current of 20 A and discharge voltage of 300 V [19]. They attributed this to decreasing beam utilization at higher currents. Based on trends seen in both previous work and our own experiment, we speculate that 2.7× the nominal current density may be around the peak in efficiency for the H9. However, the behavior beyond this peak remains an open question—will the efficiency drop precipitously or remain relatively flat? Ultimately, we will need to operate at higher current densities to resolve this question.

The observations in efficiency trends do suggest some potential strategies for how we may mitigate some of the losses, namely by improving the voltage and beam utilization efficiencies. For example, we may be able to improve the voltage utilization by increasing the discharge voltage; we operated at a constant 300 V throughout the experiment, but increasing voltage would give us a steeper potential drop and perhaps improve our efficiency. This will, however, potentially introduce more thermal issues due to the higher operating power. Similarly, we may be able to reduce the loss in beam utilization efficiency by increasing the magnetic field strength as per Eq. 4. This may also improve the voltage utilization efficiency by steepening the potential profile. However, we are already operating near the upper limit of magnetic field at 112.5% B_0 due to saturation of magnetic materials. This may place an inherent bound upon what can be achieved in terms of current utilization. Nevertheless, this slight reduction to current density at higher powers may be acceptable given the improved or at least unchanged overall efficiency, as well as the high thrust and specific impulse.

In addition to the challenges related to the efficiency, thermal stability continues to remain a potential problem for scaling to higher current densities. Indeed, while the temperature during continuous operation at 40 A remained well below values of concern, our projected steady-state temperature as shown in Fig. 10 surpasses our critical temperature. Scaling to even higher current densities would only exacerbate this problem. Resolutions to this problem may include exploring different chamber wall materials with better heat rejection, such as graphite or stainless steel. Another approach is to pulse the flow such that the thruster is not in steady-state operation. Finally, we could actively cool the thruster during testing to determine whether or not high current densities are even feasible. Doing so would allow us to explore an upper bound of current density, even if briefly, without running into major temperature concerns and the possibility of melting the anode.

Although the maximum current density we attained in this study is significantly below our goal of 10× our nominal current density, we were able to gain a deeper understanding of if and why a performance "cap" exists at high current densities, as well as potential steps we can take to mitigate it. The specific mass achieved at our highest current density is around 1.8 kg/kW, a significant improvement over the typical value of 2.4 kg/kW. We do note that as is, we would not expect the long-term operation of this thruster to be thermally stable. However, assuming that we can resolve the thermal issues through one of our identified mitigation strategies, our increased specific mass would allow us to significantly reduce our size and mass at higher powers. Scaled up in power, a 100-kW class Hall thruster would be ~180 kg with our new specific mass value; this is 80% of the 230 kg mass of the X3 [11]. Revisiting Fig. 1, if we were to increase the scaling of HETs by a factor of 2 by way of current density scaling, we would be able to achieve 100 kW with a thruster diameter of about 60 cm. This represents a 25% reduction in size compared to the X3, on par with our mass savings.

VIII. Conclusion

In summary, the goal of this work was to operate a magnetically-shielded Hall thruster at current densities that are multiple factors higher than its nominal operating value and determine how and why its performance changes. To this end, we operated a magnetically-shielded 9-kW class Hall thruster at 300 V and currents of 15 A to 40 A, 1× to 2.7× our nominal current density. We found that operation was stable (<50% discharge oscillation) and safe (no thermal concerns) for all operating conditions during the duration of the test, with some concerns regarding the long-term thermal behavior of the thruster. We showed that the thrust, specific impulse, and efficiency all increased monotonically with current, although the efficiency did see diminishing returns (i.e. smaller increases) as we approached 40 A.

By applying an efficiency model to our work and comparing the efficiency breakdown across currents, we saw that while the mass utilization efficiency increased and approached unity at 40 A, the other efficiency modes—in particular, voltage utilization—decreased at higher currents. We attributed the increasing mass utilization to shorter ionization mean free path in the channel, decreasing voltage utilization to a wider ion energy distribution function, decreasing beam utilization to increased electron transport, and decreasing charge utilization to a higher ion-to-neutral ratio in the channel. Ultimately, since the mass utilization cannot increase further, we postulate that we may have reached peak performance at 40 A for our test article. While we do not yet know how the performance would change at even higher currents, we have identified a number of potential strategies for mitigation of both efficiency losses and thermal concerns.

In terms of performance, we reached a maximum of 12 kW, 700.1 ±5.0 mN, and 65.8 ±0.9% anode efficiency on a 9-kW-class shielded Hall thruster at 2.7× its nominal operating current density. Although we have not yet closed the gap between the power densities of MPDs and HETs, we have made significant progress towards that goal and uncovered some of the possible physical drivers of performance change at high current density Hall thruster operation. This work represents an important step towards scaling Hall thrusters to the powers necessary for crewed spaceflight.

IX. Acknowledgements

This work was supported by the Graduate Research Fellowship Program from the National Science Foundation. The authors would like to thank Matthew Byrne for his assistance in testing setup and operation, Eric Viges for facility support, Thomas Marks for his guidance on curve fitting, and Dr. Richard Hofer of the Jet Propulsion Laboratory for his expertise in Hall thruster troubleshooting and testing. An additional thanks to all the members of Plasmadynamics and Electric Propulsion Laboratory for their discussions.

References

[1] "Space Nuclear Propulsion for Human Mars Exploration." Tech. rep., National Academies of Sciences, Engineering, and Medicine, Washington, DC, 2021.

[2] Brophy, J., Gershman, R., Strange, N., Landau, D., Merrill, R., and Kerslake, T., "300-kW Solar Electric Propulsion System Configuration for Human Exploration of Near-Earth Asteroids," *47th AIAA Joint Propulsion Conference*, American Institute of Aeronautics and Astronautics, AIAA-2011-5514, San Diego, CA, 2011.

[3] Strange, N., Merrill, R., Landau, D., Drake, B., Brophy, J., and Hofer, R., "Human Missions to Phobos and Deimos Using Combined Chemical and Solar Electric Propulsion," *47th AIAA Joint Propulsion Conference*, American Institute of Aeronautics and Astronautics, AIAA-2011-5663, San Diego, CA, 2011.

[4] Dankanich, J. W., Vondra, B., and Ilin, A. V., "Fast transits to Mars using electric propulsion," *46th AIAA/ASME/SAE/ASEE Joint Propulsion Conference and Exhibit*, AIAA International, 2010.

[5] Hofer, R. R., and Randolph, T. M., "Mass and cost model for selecting thruster size in electric propulsion systems," *Journal of Propulsion and Power*, Vol. 29, No. 1, 2013, pp. 166–177.

[6] Hall, S. J., Jorns, B., Gallimore, A., and Hofer, R. R., "Expanded Thruster Mass Model Incorporating Nested Hall Thrusters," *53rd AIAA/SAE/ASEE Joint Propulsion Conference*, American Institute of Aeronautics and Astronautics (AIAA), Atlanta, GA, 2017, pp. 2017–4729.

[7] Albertoni, R., Paganucci, F., Rossetti, P., and Andrenucci, M., "Experimental study of a hundred-kilowatt-class applied-field magnetoplasmadynamic thruster," *Journal of Propulsion and Power*, Vol. 29, No. 5, 2013, pp. 1138–1145.

[8] Liang, R., "The Combination of Two Concentric Discharge Channels into a Nested Hall-Effect Thruster," Ph.D. thesis, University of Michigan, Ann Arbor, MI, 2013.

[9] Hall, S., Florenz, R., Gallimore, A., Kamhawi, H., Brown, D., Polk, J., Goebel, D., and Hofer, R., "Implementation and Initial Validation of a 100-kW Class Nested-channel Hall Thruster," *Joint Propulsion Conference, AIAA-2014-3815*, American Institute of Aeronautics and Astronautics, Cleveland, OH, 2014.

[10] Florenz, R., Gallmiore, A., and Peterson, P., "Developmental Status of a 100-kW Class Laboratory Nested channel Hall Thruster," *32nd International Electric Propulsion Conference*, Wiesbaden, Germany, 2011, pp. 2011–246.

[11] Hall, S. J., Jorns, B. A., Gallimore, A. D., Kamhawi, H., Haag, T. W., Mackey, J. A., Gilland, J. H., Peterson, P. Y., and Baird, M. J., "High-Power Performance of a 100-kW Class Nested Hall Thruster," *35th International Electric Propulsion Conference*, Atlanta, GA, 2017, pp. 2017–228.

[12] Cusson, S., Hall, S., Hofer, R., Jorns, B., and Gallimore, A., "The Impact of Magnetic Field Coupling Between Channels in a Nested Hall Thruster," *35th International Electric Propulsion Conference*, Atlanta, Georgia, 2017, pp. 2017–507.

[13] Moore, C., Pencil, E., Hardy, R., Bollweg, K., and Ching, M., "NASA's NextSTEP Advanced Electric Propulsion Activities," *AIAA Propulsion and Energy Forum*, 2018.

[14] Jorns, B., Gallimore, A., Hall, S., Peterson, P., Gilland, J., Goebel, D., Hofer, R., and Mikellides, I., "Update on the Nested Hall Thruster Subsystem for the NextSTEP XR-100 Program," *Joint Propulsion Conference, AIAA-2018-4418*, American Institute of Aeronautics and Astronautics, Cincinnati, OH, 2018.

[15] Hall, S. J., "Characterization of a 100-kW Class Nested-Channel Hall Thruster," Ph.D. thesis, University of Michigan, Ann Arbor, MI, 2018.

[16] Shark, S. W., Hall, S. J., Jorns, B. A., Hofer, R. R., and Goebel, D. M., "High Power Demonstration of a 100 kW Nested Hall Thruster System," *AIAA Propulsion and Energy 2019 Forum*, Indianapolis, IN, 2019.

[17] Dannenmayer, K., and Mazouffre, S., "Elementary scaling relations for hall effect thrusters," *Journal of Propulsion and Power*, Vol. 27, No. 1, 2011, pp. 236–245.

[18] Grishin, S., Erofeev, V., Zharinov, A., Naumkin, V., and Safronov, I., "Characteristics of a Two-stage Ion Accelerator with an Anode Layer," *Zhurnal Prikladnoi Mekhaniki i Tekhnicheskoi Fiziki*, Vol. 2, 1978, pp. 28–36.

[19] Reid, B. M., "The Influence of Neutral Flow Rate in the Operation of Hall Thrusters," Ph.d. dissertation, University of Michigan, Ann Arbor, MI, 2009.

[20] Mikellides, I. G., Katz, I., Hofer, R. R., and Goebel, D. M., "Magnetic shielding of a laboratory Hall thruster. I. Theory and validation," *Journal of Applied Physics*, Vol. 115, No. 4, 2014.

[21] Hofer, R. R., Goebel, D. M., Mikellides, I. G., and Katz, I., "Magnetic shielding of a laboratory Hall thruster. II. Experiments," *Journal of Applied Physics*, Vol. 115, No. 4, 2014.

[22] Hofer, R., Goebel, D., Mikellides, I., and Katz, I., "Design of a Laboratory Hall Thruster with Magnetically Shielded Channel Walls, Phase II: Experiments," *48th AIAA/ASME/SAE/ASEE Joint Propulsion Conference & Exhibit*, American Institute of Aeronautics and Astronautics, Atlanta, GA, 2012.

[23] Hofer, R. R., and Gallimore, A. D., "Efficiency Analysis of a High-Specific Impulse Hall Thruster," *40th Joint Propulsion Conference, AIAA-2004-3602*, American Institute of Aeronautics and Astronautics, Ft. Lauderdale, FL, 2004.

[24] Hofer, R. R., "Development and Characterization of High-Efficiency, High-Specific Impulse Xenon Hall Thrusters," Ph.D. thesis, University of Michigan, 2004.

[25] Hofer, R. R., Katz, I., Mikellides, I. G., Goebel, D. M., Jameson, K. K., Sullivan, R. M., , and Johnson, L. K., "Efficacy of Electron Mobility Models in Hybrid-PIC Hall Thruster Simulations," *44th Joint Propulsion Conference, AIAA-2008-4924*, American Institute of Aeronautics and Astronautics, Hartford, CT, 2008.

[26] Hofer, R. R., Cusson, S. E., Lobbia, R. B., and Gallimore, A. D., "The H9 Magnetically Shielded Hall Thruster," *35th International Electric Propulsion Conference*, Atlanta, GA, 2017.

[27] Myers, R. M., "Geometric scaling of applied-field magnetoplasmadynamic thrusters," *Journal of Propulsion and Power*, Vol. 11, No. 2, 1995, pp. 343–350.

[28] Cassady, L., Longmier, B., Olsen, C., Ballenger, M., McCaskill, G., Illin, A., Carter, M., Glover, T., Squire, J., Chang Diaz, F., Diaz, C., and Bering, E., "VASIMR Performance Results," American Institute of Aeronautics and Astronautics (AIAA), 2010.

[29] Polk, J. E., Anderson, J. R., Brophy, J. R., Rawlin, V. K., Patterson, M. J., Sovey, J., and Hamley, J., "An overview of the results from an 8200 hour wear test of the NSTAR ion thruster," *35th Joint Propulsion Conference and Exhibit*, American Institute of Aeronautics and Astronautics Inc, AIAA, 1999.

[30] Patterson, M. J., and Benson, S. W., "NEXT ion propulsion system development status and performance," *Collection of Technical Papers - 43rd AIAA/ASME/SAE/ASEE Joint Propulsion Conference*, Vol. 2, 2007, pp. 1913–1929. https://doi.org/10.2514/6.2007-

5199.
[31] Boeuf, J. P., "Tutorial: Physics and modeling of Hall thrusters," *Journal of Applied Physics*, Vol. 121, No. 1, 2017. https://doi.org/10.1063/1.4972269.
[32] Goebel, D. M., and Katz, I., *Fundamentals of Electric Propulsion: Ion and Hall Thrusters*, Jet Propulsion Laboratory, California Institute of Technology, Pasadena, CA, 2008.
[33] Su, L. L., Vazsonyi, A. R., and Jorns, B., "Performance of a 9-kW Magnetically-Shielded Hall Thruster with Krypton," *Propulsion and Energy Forum*, American Institute of Aeronautics and Astronautics (AIAA), 2020.
[34] Cusson, S. E., Hofer, R. R., Lobbia, R., Jorns, B. A., and Gallimore, A. D., "Performance of the H9 Magnetically Shielded Hall Thrusters," *35th International Electric Propulsion Conference*, Atlanta, Georgia, 2017.
[35] Hofer, R. R., Goebel, D. M., and Walker, R. M., "Compact Lab6 Hollow Cathode for a 6-kW Hall Thruster," *54th JANNAF Propulsion Meeting*, 2018, pp. 14–17.
[36] Dankanich, J. W., Walker, M., Swiatek, M. W., and Yim, J. T., "Recommended practice for pressure measurement and calculation of effective pumping speed in electric propulsion testing," *Journal of Propulsion and Power*, Vol. 33, No. 3, 2017, pp. 668–680. https://doi.org/10.2514/1.B35478.
[37] Cusson, S. E., Dale, E. T., Jorns, B. A., and Gallimore, A. D., "Acceleration region dynamics in a magnetically shielded Hall thruster," *Physics of Plasmas*, Vol. 26, No. 2, 2019.
[38] Sheehan, J. P., Raitses, Y., Hershkowitz, N., and McDonald, M., "Recommended practice for use of emissive probes in electric propulsion testing," *Journal of Propulsion and Power*, Vol. 33, No. 3, 2017, pp. 614–637.
[39] Lobbia, R. B., and Beal, B. E., "Recommended Practice for Use of Langmuir Probes in Electric Propulsion Testing," *Journal of Propulsion and Power*, Vol. 33, No. 3, 2017, pp. 566–581. https://doi.org/10.2514/1.B35531.
[40] Huang, W., Shastry, R., Soulas, G. C., and Kamhawi, H., "Farfield Plume Measurement and Analysis on the NASA-300M and NASA-300MS," *33rd International Electric Propulsion Conference*, Washington D.C., USA, 2013.
[41] Brown, D. L., Walker, M. L., Szabo, J., Huang, W., and Foster, J. E., "Recommended practice for use of faraday probes in electric propulsion testing," *Journal of Propulsion and Power*, Vol. 33, No. 3, 2017, pp. 582–613.
[42] Hagstrum, H. D., "Auger Ejection of Electrons from Molybdenum by Noble Gas Ions," *Physical Review*, Vol. 104, No. 3, 1956.
[43] Hagstrum, H. D., "Auger Ejection of Electrons from Tungsten by Noble Gas Ions," *Physical Review*, Vol. 96, No. 2, 1954.
[44] Haas, J. M., "Low-Perturbation Interrogation of the Internal and Near-Field Plasma Structure of a Hall Thruster Using a High-Speed Probe Positioning System," Ph.D. thesis, University of Michigan, Ann Arbor, 2001.
[45] Brown, D. L., and Gallimore, A. D., "Evaluation of Facility Effects on Ion Migration in a Hall Thruster Plume," *Journal of Propulsion and Power*, Vol. 27, No. 3, 2011, pp. 573–585.
[46] Frieman, J. D., Liu, T. M., and Walker, M. L. R., "Background Flow Model of Hall Thruster Neutral Ingestion," *Journal of Propulsion and Power*, Vol. 33, 2017, pp. 1087–1101.
[47] Peterson, P., Jacobson, D., Manzella, D., and John, J., "The Performance and Wear Characterization of a High-Power High-Isp NASA Hall Thruster," *41st AIAA/ASME/SAE/ASEE Joint Propulsion Conference & Exhibit*, American Institute of Aeronautics and Astronautics (AIAA), Tucson, AZ, 2005, pp. 2005–4243.
[48] Morozov, A. I., and Savelyev, V. V., "Fundamentals of Stationary Plasma Thruster Theory," *Reviews of Plasma Physics*, Vol. 21, 2000, pp. 203–391.